RSC Advances

PAPER

View Article Online
View Journal | View Issue

Cite this: RSC Adv., 2017, 7, 11000

High volumetric energy density annealed-MXene-nickel oxide/MXene asymmetric supercapacitor†

Qi Xun Xia,[a] Jianjian Fu,[a] Je Moon Yun,*[b] Rajaram S. Mane[b] and Kwang Ho Kim*[ab]

Received 7th December 2016
Accepted 7th February 2017

DOI: 10.1039/c6ra27880a

rsc.li/rsc-advances

A $Ti_3C_2T_x$ MXene electrode decorated with NiO nanosheets was synthesized by a facile and cost-effective hydrothermal method. The NiO nanosheets were grown and immobilized on the carbon-supported TiO_2 layer which was derived from $Ti_3C_2T_x$-MXene during a thermal annealing process. An electrode based on the NiO-grown derived-TiO_2/C-$Ti_3C_2T_x$-MXene nanocomposite (Ni-dMXNC) exhibited a remarkable maximum specific capacity of 92.0 mA h cm^{-3} at 1 A g^{-1} and 53.9 mA h cm^{-3} at 10 A g^{-1}. Furthermore, an asymmetric supercapacitor (ASC) device composed of Ni-dMXNC as the positive electrode and $Ti_3C_2T_x$ MXene as the negative electrode was demonstrated to be better with a high energy density of 1.04×10^{-2} W h cm^{-3} at a power density of 0.22 W cm^{-3}, and cycling stability with 72.1% retention after 5000 cycles, compared to ASCs using previously reported $Ti_3C_2T_x$ MXene materials. The enhanced capacitive performance is attributed to the newly formed high-surface-area multilayers of the Ni-dMXNC architecture, the active surface of NiO layer, and a favourable synergetic behaviour of the $Ti_3C_2T_x$ MXene negative electrode.

1. Introduction

Since the discovery of graphene,[1,2] two-dimensional (2D) materials with very high aspect ratios and thicknesses of a few atomic layers have attracted significant attention. They have numerous applications in electronic, photonic, and energy storage devices.[3–7] Among the available 2D materials, graphene has received considerable attention in the energy storage sector because it has excellent electrochemical properties.[8–10] The unusual properties of 2D materials such as graphene and MoS_2 have inspired researchers to investigate other 2D materials. One new family of 2D materials, labelled MXenes,[11] has shown various unusual properties compared to previously reported 2D materials like MoS_2, graphene, and phosphorene.[12–14] These MXenes are produced by selective etching of the A layers from a layered MAX material with the structural formula $M_{n+1}AX_n$, where M is an early transition metal, A is mostly IIIA- and IVA-group elements, X is carbon and/or nitrogen, and $n = 1$, 2, or 3.[15,16]

The MXene group of materials displays unusual combined metallic conductivity and hydrophobicity, excellent chemical, thermal, and environmental stabilities, and excellent mechanical properties,[11,17] for which they are under investigation as anode materials in Li-ion batteries[18,19] and supercapacitors.[20,21] Supercapacitors are considered among the most promising energy storage devices because they have fast charge and discharge rates, high power densities, long cycle lifetimes, and greater reliability than Li-ion batteries.[22–24] Rakhi *et al.* explored $Ti_3C_2T_x$ MXene electrodes with the specific capacitance of 51 F g^{-1} in an electrolyte of 30 wt% KOH and a current density of 1 A g^{-1}.[25] Recently, Lin *et al.* reported on a 2D $Ti_3C_2T_x$ MXene electrode with 117 F g^{-1} at a scan rate of 2 mV s^{-1} in 1 M KOH electrolyte.[26] However, for the portable electronics and vehicles, the areal and volumetric performances are two important indicators for supercapacitors.[27] The volumetric performance reflects how large and fast energy can be stored in a unit volume of materials/packed device, which indicates more reliable and precise parameter for evaluating the charge-storage capacity of supercapacitor compared with that of gravimetric performance.[28,29] MXene electrode materials display significantly higher volumetric capacitances compared to previously reported carbon-based materials, which have capacitances limited to 60 F cm^{-3}.[30] The high packing density of MXenes described it as a promising electrode material for energy storage devices with high volumetric energy and power densities.[31]

In continuation of our ongoing positive and negative electrode materials research, in this work we have synthesized

[a]School of Materials Science and Engineering, Pusan National University, San 30 Jangjeon-dong, Geumjeong-gu, Busan 609-735, Republic of Korea. E-mail: kwhokim@pusan.ac.kr

[b]Global Frontier R&D Center for Hybrid Interface Materials, Pusan National University, San 30 Jangjeon-dong, Geumjeong-gu, Busan 609-735, Republic of Korea. E-mail: yunjemoon@gmail.com

† Electronic supplementary information (ESI) available: FESEM images of Ti_3AlC_2 MAX phase, $Ti_3C_2T_x$ MXene and NiO, EDX of Ni-dMXNC, TEM images of NiO nanosheets, adsorption–desorption isotherms of $Ti_3C_2T_x$ MXene and Ni-dMXNC, CV curves of $Ti_3C_2T_x$ MXene and Ni-dMXNC, Fig. S1–S8. Resistivity of the $Ti_3C_2T_x$ MXene and Ni-dMXNC materials, Table S1. Comparison of maximum gravimetric capacity and volumetric capacity of the reported MXene-based materials and the present work, Table S2. See DOI: 10.1039/c6ra27880a

carbon-supported TiO_2 on $Ti_3C_2T_x$ MXene surface area, which called derived TiO_2/C-$Ti_3C_2T_x$-MXene by an oxidation process. Compare with the $Ti_3C_2T_x$-MXene, the derived TiO_2/C-$Ti_3C_2T_x$-MXene displaying higher conductivity and bigger specific surface area,[32] which are of great importance and considered to be the key factors in improving the performance of supercapacitors. The derived TiO_2/C-$Ti_3C_2T_x$-MXene electrodes decorated with NiO nanosheets, named derived TiO_2/C-$Ti_3C_2T_x$-MXene/NiO nanocomposite (Ni-dMXNC) electrodes, and tested them as potential positive electrode materials. They demonstrated higher performances than previously reported MXenes.

In the MXene family, Ti_3C_2 is one of the lightest members. We selected Ti_3C_2 MXene as the basis for this contribution. The Ti_3C_2-based MXene powders were synthesized by etching Al from the Ti_3AlC_2 MAX phase. The as-obtained Ti_3C_2 surface was then terminated with functional groups, such as –OH, =O, and –F; for simplicity, in this text we utilize the chemical formula "$Ti_3C_2T_x$" to represent the as-produced surface-terminated MXene, where T represents the terminating groups and x is the number of groups per Ti_3C_2 unit cell. Herein, we report for the first time the superior electrochemical performance of a Ni-dMXNC//$Ti_3C_2T_x$ MXene asymmetric supercapacitor (ASC) device relative to the previously reported symmetric supercapacitors (SSCs) with $Ti_3C_2T_x$ MXene-based electrodes. This demonstrates the superiority of the composited $Ti_3C_2T_x$ MXene in energy storage devices relative to $Ti_3C_2T_x$ MXene alone; this superiority may be valid for other MXene materials too.

2. Experiment section

2.1. Materials

Concentrated hydrochloric acid (37 wt%, HCl), and concentrated hydrofluoric acid (48–51 wt%, HF) were obtained from Daejung Chemicals (Korea). Acetone and anhydrous ethanol were supplied by SK Chemical (Korea). All other chemicals were of analytical grade, purchased from Sigma-Aldrich and used as received.

2.2. Synthesis of bulk Ti_3AlC_2

Ti powder (99.9 wt% purity, 300 mesh), Al powder (99.9 wt% purity, 300 mesh), and graphite powder (99.9 wt% purity, 300 mesh) were mixed in the molar ratio of Ti : Al : C = 3 : 1 : 2 for 12 h in a planetary ball mill machine. Then the MAX, *i.e.* Ti_3AlC_2, as the precursor of the MXene $Ti_3C_2T_x$, was obtained through the chemical reaction

$$3Ti + Al + 2C \rightarrow Ti_3AlC_2 \quad (1)$$

by a spark plasma sintering process of heating the powder at 1200 °C for 10 min under a pressure of 30 MPa. To obtain the Ti_3AlC_2 powder, ball-milling was performed on the spark plasma-sintered Ti_3AlC_2 for 12 h.

2.3. Synthesis of $Ti_3C_2T_x$ powder

The Ti_3AlC_2 powder was immersed in concentrated HF (50 wt%) solution at room temperature for 24 h to extract the Al atoms. The suspension was poured into a 45 mL centrifuge tube, centrifuged at 3500 rpm for 5 min, and washed with deionized (DI) water 5 times to remove the HF acid. It was then exfoliated into few-layer flakes by dimethyl sulfoxide (DMSO) intercalation and weak sonication. Finally, the flakes were washed with DI water several times and dried at 50 °C for 12 h to obtain the $Ti_3C_2T_x$ MXene powder product.

2.4. Preparation of the Ni-dMXNC

The precursor for the growth of nickel hydroxide ($Ni(OH)_2$) was prepared as described in our previous report.[33] In particular, 1.45 g $Ni(NO_3)_2 \cdot 6H_2O$ (100 mmol), 0.18 g hexamethylenetetramine (25 mmol), and 1 g $Ti_3C_2T_x$ MXene powder were dispersed in 50 mL DI water, mixed homogeneously under ultrasonication for 30 min at room temperature, poured into a 50 mL Teflon autoclave, and kept at 90 °C for 4 h. The $Ti_3C_2T_x$ MXene covered with $Ni(OH)_2$ was washed with DI water and ethanol to remove surface ions and molecules before being vacuum-dried at 50 °C for 12 h. For converting $Ni(OH)_2$ to NiO, the assembly was annealed at 400 °C for 1 h. We found that the as-obtained product differed from the $Ti_3C_2T_x$ MXene and referred to it as a derived TiO_2/C-$Ti_3C_2T_x$-MXene/NiO nanocomposite (Ni-dMXNC).

2.5. Preparation of the Ni-dMXNC electrode

A Ni foam of 1 cm × 1 cm area, 110 PPI pore density, and 320 g m^{-2} mass density (Artenano Company Limited, Hong Kong) was thoroughly cleaned before experimental use through the following steps. It was degreased by immersion in acetone for 30 min; etched with dilute HCl (3.0 mol L^{-1}) for 15 min, and rinsed with DI water before drying. The working electrode slurry was made by mixing the Ni-dMXNC powder, carbon black, and a binder of polytetrafluoroethylene (PTFE) suspension (60 wt%) at a weight ratio of 8 : 1 : 1. All were pasted to the 1 cm × 1 cm Ni foam area and pressed at 30 MPa. The electrode was then dried at 50 °C in vacuum for 12 h and used as an electrode in the rest of the measurements. To prepare the $Ti_3C_2T_x$ MXene electrode, the same procedure was adopted, but except NiO. While monitoring the mass density of the Ni-dMXNC and $Ti_3C_2T_x$ powders amounts of equal mass were cold-pressed into 10 mm-diameter separate thin discs under 30 MPa pressure.

2.6. Materials characterizations

The phases of the as-deposited and modified $Ti_3C_2T_x$ MXene were characterized by X-ray diffraction (XRD, D8-Discovery Bruker, Cu Kα, 40 kV, 40 mA). Scanning electron microscopy (SEM, Hitachi, S-4800, 15 kV) and transmission electron microscopy (HRTEM, Tecnai F20) plane-view digital photographs were used to observe the surface changes of $Ti_3C_2T_x$ MXene. X-ray photoelectron spectroscopy (XPS, VG Scientific ESCALAB250) was utilized to analyse the chemical bonding status of the Ni-dMXNC. The XPS spectrum of the Ni-dMXNC was calibrated to the carbon peak C 1s at 284.6 eV. To verify the electric conductivities of MXene and Ni-dMXNC materials respectively, they were prepared with those discs (10 mm in diameter, ~0.4 mm thick under a 30 MPa pressing process) and measured for those resistances using Hall-effect measurement system (ECOPIA, HMS-3000 with four-probe technique).

2.7. Electrochemical performance measurements

The electrochemical tests from half-cell measurements were performed under a three-electrode electrochemical system in an electrolyte of 1 M KOH at room temperature. A Pt plate and Hg/HgO were used as the counter and reference electrode, respectively. Cyclic voltammetry (CV) measurements and galvanostatic charge/discharge tests were performed on an Ivium-n-Stat electrochemical workstation (Ivium, Netherlands). The specific discharge capacity value of the electrode was calculated using the following eqn (2)[34]

$$Q_D = \frac{I\Delta t}{m} \quad (2)$$

where Q_D is in mA h g^{-1}, I (A) is the applied current, m (g) is the designated mass (of the active materials), and Δt (s) is the discharge durations.

In order to observe the potential change of each electrode, a Ni-dMXNC material (positive electrode) and a $Ti_3C_2T_x$ MXene material (negative electrode) were placed face-to-face and measured in 1 M KOH. The mass ratio of the active materials (Ni-dMXNC : $Ti_3C_2T_x$) was estimated to be 1 : 4.39. The GCD curves of asymmetric cells with the potential change of each individual electrode were monitored *in situ* by an auxiliary channel and a reference electrode (mercury/mercury oxide).[35]

2.8. Fabrication of the ASC

The ASC with Ni-dMXNC//$Ti_3C_2T_x$ MXene configuration was assembled using the Ni-dMXNC and $Ti_3C_2T_x$ MXene as the positive electrode and negative electrode, respectively. Based on the charge balance theory and as discussed above, the mass ratio of the active materials (Ni-dMXNC : $Ti_3C_2T_x$) was estimated at 1 : 4.39. The Ni-dMXNC and $Ti_3C_2T_x$ MXene electrodes were separated with a cellulose paper separator. CR2032 coin-cell packaging was used in assembling the devices. An electrolyte of 1 M KOH was used, introduced over or into each electrode before fixing the coin cell for the ASC using a hydraulic coin-cell sealing machine (Shenzhen Pengxiangyunda Machinery, PX-HS-20). The specific discharge capacity (mA h g^{-1}) of the ASC device (Q_D) was calculated from the GCD curves according to eqn (3),

$$Q_D = \frac{I\Delta t}{M} \quad (3)$$

where I (A) is the applied current, Δt (s) is the time required for discharge, and M (g) is the total mass of the active materials *i.e.*, the positive and negative electrodes.

The energy density (W h cm^{-3}) and power density (W cm^{-3}) values of the Ni-dMXNC//$Ti_3C_2T_x$ ASC, as derived from the GCD curves, were calculated using the following equations:[34,36]

$$E = \frac{I\int V\,dt}{3.6M} \quad (4)$$

$$V = m_p/\rho_p + m_n/\rho_n \quad (5)$$

$$P = E/\Delta t \quad (6)$$

where E (W h cm^{-3}) is the energy density, I is the applied current, V is the total volume of both positive and negative electrodes, $\int V dt$ is the galvanostatic discharge current area, m_p and m_n is mass of positive and negative electrodes, ρ_p and ρ_n is the mass density of positive and negative electrodes, respectively. P (W cm^{-3}) is the power density, and Δt (s) is the discharge time.

3. Results and discussion

3.1. Physicochemical characterization

A schematic of $Ti_3C_2T_x$ synthesis with exfoliation is shown in Scheme 1. In the first step, Ti_3AlC_2 powder is etched using concentrated HF (50 wt%) at room temperature for 24 h to remove the Al layers present therein. In the second step, the MXene is exfoliated into few-layer flakes by DMSO intercalation and weak sonication. The Ni-dMXNC obtained by this facile hydrothermal method after annealing shows a different structure and surface morphology than $Ti_3C_2T_x$ MXene.

Side-view surface field-emission SEM (FESEM) images of the obtained Ti_3AlC_2 MAX phase and the $Ti_3C_2T_x$ MXene are shown in Fig. S1 (ESI†). Fig. S1a† illustrates the synthesized crushed MAX powders with clearly laminar shapes. It is difficult to estimate the exact plate thickness of individual sheets, but groups of sheets are 40–200 nm in thickness. Fig. S1b† shows that the $Ti_3C_2T_x$ MXene surface, after HF treatment, is typically delaminated from MXene with a thickness of 40–220 nm. In

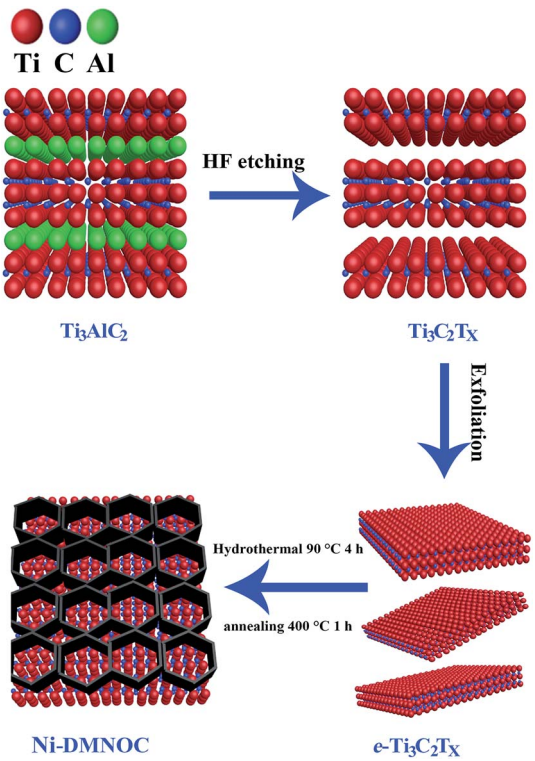

Scheme 1 Schematic of the preparation of the Ni-dMXNC by facile hydrothermal method.

order to increase the interlayer spacing of the $Ti_3C_2T_x$ MXene, the bonds between the $Ti_3C_2T_x$ MXene layers were weakened by DMSO intercalation. The exfoliated $Ti_3C_2T_x$ MXene obtained by DMSO treatment is shown in Fig. 1a, which features larger slots than before the DMSO exfoliation of the $Ti_3C_2T_x$ MXene. As the single layer of $Ti_3C_2T_x$ MXene flakes is 1 nm thick,[37] as-obtained $Ti_3C_2T_x$ MXene flakes by DMSO treatment are approximately 10–70 nm thick, corresponding to 10–70 layers multilayer. The FESEM image of the Ni-dMXNC shown in Fig. 1b demonstrates the increased dimensions (horizontal as well as vertical) of individual nanosheets and the growth of vertical NiO nanosheets between horizontally stacked modified $Ti_3C_2T_x$ MXene layers, suggesting the successful addition of the NiO nanosheets. The flower-like NiO composed of several nanosheets is confirmed in Fig. S4a,† which shows hierarchical microspheres. The electrical properties of pure $Ti_3C_2T_x$ MXene and Ni-dMXNC determined from using Hall-effect measurement system, as shown in Table S1 (ESI†). From the resistance measurements of $Ti_3C_2T_x$ MXene and Ni-dMXNC, it is clearly indicated that the conductivity of Ni-dMXNC is superior to pure $Ti_3C_2T_x$ MXene. With the combined features of the modified $Ti_3C_2T_x$ MXene and NiO, the composite have the increased surface area and the active NiO covering, thus increasing electrode/electrolyte interfacial contact area, shortening diffusion paths for both electrons and ions, and improving conductivity; any of these may improve the electrochemical performance compared to those of pristine and modified $Ti_3C_2T_x$ MXene. Fig. 1c demonstrates the typical XRD patterns of the MAX before and after HF treatment, showing a phase change from MAX to $Ti_3C_2T_x$ MXene. The well-defined diffraction peaks observed at 2θ values of 9.2°, 19.2°, 34.0°, 36.7°, 39.0°, 41.8°, 48.5°, 52.4°, 56.6°, 60.2°, 65.6°, 70.5°, and 74.1° are indexed to the (002), (004), (100), (103), (104), (105), (107), (108), (109), (110), (1011), (118) and (1013) planes, respectively, of the MAX Ti_3AlC_2 (JCPDS 52-0875). After etching, almost all Al is removed from this structure; the (002) and (004) planes of the MAX phase are shifted to lower angles, indicating larger d spacings in MXene than in MAX.[11] For the XRD pattern of MXene, it can be found that there are some peaks of TiO_2 at ~25°, 37° and 47° (Fig. 1c), indicating that MXene has been partially oxidized. The XRD pattern of Ni-dMXNC (Fig. 1d) shows the presence of anatase TiO_2 peaks (01-071-1167), indicating that TiO_2 derived from $Ti_3C_2T_x$ MXene during the annealing and hydrothermal process.[38] TiO_2 is an outstanding electrode materials in energy storage due to its low potential, good cycle stability and fast lithium intercalation.[39,40] So, the derived TiO_2 hold great promise on improving the electrochemical performance of MXene-based electrode materials. New peaks at 2θ values of 37.1°, 43.2°, 62.9°, 75.2°, and 79.6° were assigned to the (111), (200), (220), (311), and (222) planes of NiO (JCPDS 01-078-0643).

To investigate the formation mechanism and the spatial distributions of corresponding elements of the Ni-dMXNC, elemental mappings were performed (Fig. 2). The elemental mapping displays the uniform coverage of Ni on the modified $Ti_3C_2T_x$ MXene. In Fig. S2,† the energy dispersive X-ray spectroscopy (EDS) analyses of $Ti_3C_2T_x$ MXene and Ni-dMXNC clearly reveal the corresponding elemental contents with an atomic ratio. The $Ti_3C_2T_x$ MXene contains T, C, F, O elements with an atomic ratio of Ti : C : O : F = 27 : 15 : 11 : 10 (Fig. S2e†). The selected area EDS of Ni-dMXNC (Fig. S2d†)

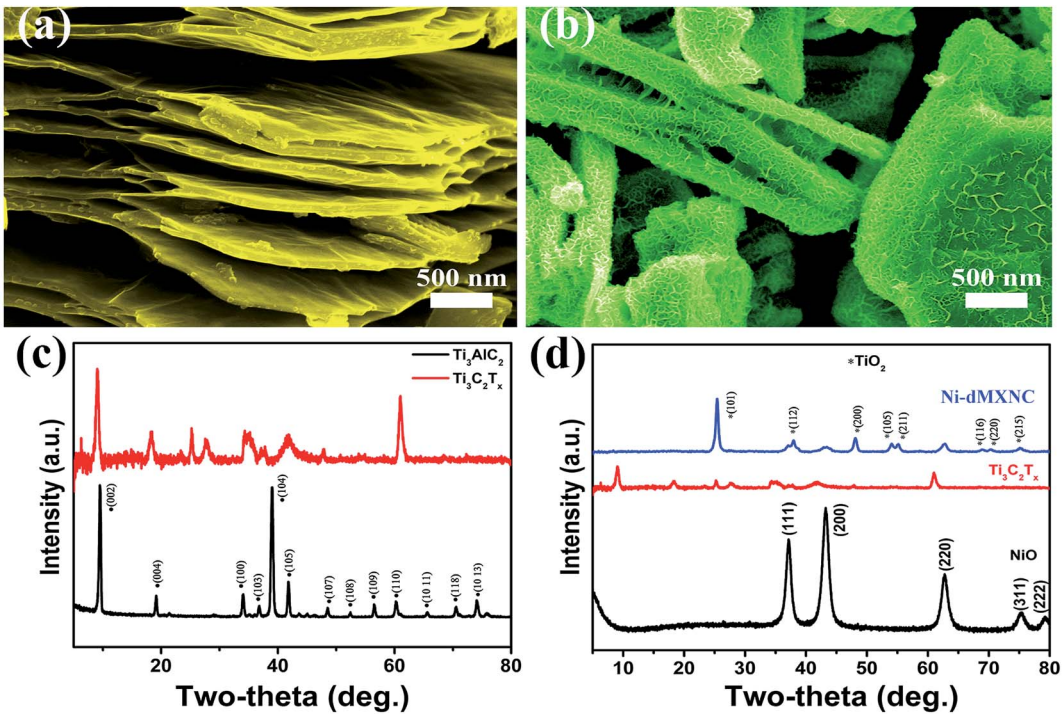

Fig. 1 SEM images of the (a) as-obtained $Ti_3C_2T_x$ MXene after DMSO treatment, and (b) the as-obtained Ni-dMXNC. (c) XRD patterns of pre-HF-treated Ti_3AlC_2 MAX phase and post-HF treated $Ti_3C_2T_x$ MXene. (d) XRD patterns of NiO nanosheets, $Ti_3C_2T_x$ MXene, and Ni-dMXNC.

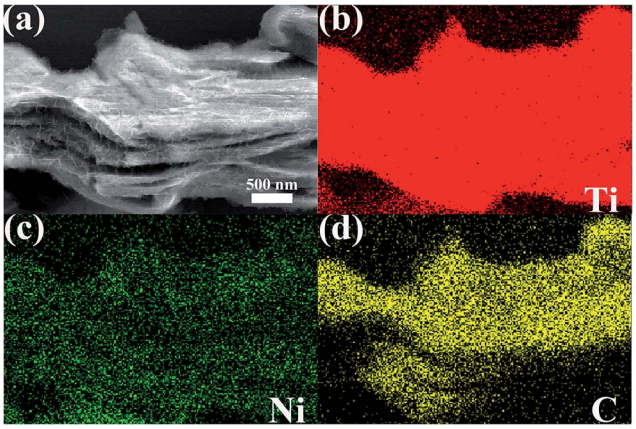

Fig. 2 (a) Microstructure and chemistry of Ni-dMXNC. EDS mapping of (b) Ti, (c) Ni, and (d) C.

comprises Ni, O, C, and Ti. The corresponding elemental contents in Fig. S2f† reveal that the main constituents are Ti, C, Ni, and O with an atomic ratio of Ti : C : Ni : O = 34 : 14 : 10 : 34. Note that the C content lower than the stoichiometric of the Ti_3C_2 may be attributed to the production of carbon dioxide by the oxidization of carbon element along with the oxidization of other elements. The Ti : Ni atomic ratio of the as-obtained Ni-dMXNC is calculated at 3.4 : 1.

High-resolution XPS measurements were utilized to characterize the chemical composition and valence states of the elements in pure MXene (Fig. S3†) and Ni-dMXNC (Fig. 3). In the Ti 2p spectrum (Fig. S3a†), Ti 2p core level was fitted with two doublets (Ti $2p_{3/2}$–Ti $2p_{1/2}$) with a fixed area ratio equal to 2 : 1 and a doublet separation of 5.7 eV. The Ti $2p_{3/2}$ components were located at 455.0 eV and 456.2 eV, which corresponding to Ti–C and Ti–X bond, respectively.[41,42] Ti $2p_{1/2}$ components were located at 460.8 eV and 462.7 eV corresponding to C–Ti–O_x and Ti–O, respectively.[43] The C 1s (Fig. S3b†) peaks at 281.1 eV and 284.6 eV corresponding to Ti–C and C–C bond, respectively.[41,44] The O 1s spectrum (Fig. S3c†) are fitted using 2 components located at 529.8 eV and 531.8 eV corresponding to O 1s in TiO_2 and hydroxyl groups.[45] The F 1s XPS (Fig. S3d†) shows a predominant peak at 863.7 eV, corresponding to Ti_3C_2F.

The high-resolution XPS spectra Ti 2p and C 1s of Ni-dMXNC were presented in Fig. 3b and c. Ti 2p core level was fitted with two doublets (Ti $2p_{3/2}$–Ti $2p_{1/2}$) with a fixed area ratio equal to 2 : 1 and a doublet separation of 5.7 eV. The Ti $2p_{3/2}$ peak located at 455.0 eV corresponds to Ti–C in the core. The 458.0 eV (Ti $2p_{3/2}$) and 463.7 eV (Ti $2p_{1/2}$) peaks are ascribed to Ti–O on the surface.[46,47] The Ti–O is from the oxidation of MXene (TiO_2). The C 1s (Fig. 3c) peaks at 281.0 eV, 284.6 eV, and 286.0 eV are assigned to the characteristic bonds of C–Ti, C–C, and C–O, respectively.[44] The Ni 2p spectrum, as shown in Fig. 3d, presents two obvious satellites (indicated as "Sat") and Ni $2p_{3/2}$ and Ni $2p_{1/2}$ peaks at 855.9 eV and 873.6 eV, both supporting the presence of Ni^{2+}. We observe two O environments of NiO in the O 1s XPS (Fig. 3e): the O 1s peak located at 529.3 eV is ascribed to O–Ni and that at 531.1 eV to O–H, confirming the presence of several hydroxyl groups (Ti–OH) to form the $Ti_3C_2(OH)_2$ covering the $Ti_3C_2T_x$ MXene surface.[6] The F 1s XPS (Fig. 3f) shows a predominant peak at 863.7 eV, corresponding to Ti_3C_2F. These results clearly show the abundance of functional groups and the availability of electroactive sites like –OH, –F, Ti^{4+}, and Ni^{2+} in Ni-dMXNC, which are conducive to the high rate capacity and long-range cycling stability of supercapacitors.

The typical morphological and structural characterizations were further investigated by TEM (Fig. 4 and S4†). Fig. S4a (ESI†) shows the NiO nanosheets in a hierarchical porous sphere shape. In the high-resolution TEM (HRTEM) image (Fig. S4b, ESI†), a 0.207 nm lattice fringe spacing for NiO (200) is evidenced; in the corresponding selected-area electron diffraction (SAED) pattern (Fig. S4c, ESI†), polycrystallinity is verified. The exfoliated $Ti_3C_2T_x$ MXene, as seen in Fig. 4a–c, presents a 0.352 nm lattice fringe spacing corresponding to anatase TiO_2 (101) and the corresponding SAED patterns shows the hexagonal symmetry of the flakes and single-crystal nature of the modified $Ti_3C_2T_x$ MXene,[48–50] suggesting that the TiO_2 particles are nucleated on the external or interior $Ti_3C_2T_x$ MXene layers, which agrees well with the $Ti_3C_2T_x$ MXene XRD analysis. Fig. 4d–f provides structural information on the Ni-dMXNC. The low-magnification TEM image shows that NiO nanosheets grow on the $Ti_3C_2T_x$ MXene. The SAED pattern of the corresponding HRTEM image of the Ni-dMXNC is shown in Fig. 4f and corroborates the polycrystalline nature of the modified MXene. The TEM results agree well with the above XRD and XPS measurements.

To further investigate the surface properties of the Ni-dMXNC, Brunauer–Emmett–Teller (BET) results are presented in Fig. S5 (ESI†) A typical type-IV isothermal and an H3-type hysteresis loop in the relative pressure (P/P_o) range of 0.5–1.0 are obtained. These indicate the formation of slit-like pores in the Ni-dMXNC mesoporous structure. The presence of two peaks at 3 and 20 nm in the pore-size distribution plot indicates excess mesoscale pores.[51,52] The specific surface areas, pore size, and total pore volumes of the $Ti_3C_2T_x$ MXene and Ni-dMXNC are, respectively, 10.0 $m^2\ g^{-1}$ and 77.5 $m^2\ g^{-1}$, 24.1 nm and 21.1 nm, and 0.02 $cm^3\ g^{-1}$ and 0.20 $cm^3\ g^{-1}$ (Table 1), suggesting the superiority of the latter relative to the former. The high surface area of the Ni-dMXNC could enhance its electrochemical properties, as the pore channels facilitate rapid electrolyte transportation to the surface of the active materials. In addition, the defects formed during the phase change could provide more active sites for redox reactions.[53]

3.2. Electrochemical evaluation

The electrochemical performances of the $Ti_3C_2T_x$ MXene and Ni-dMXNC electrodes were evaluated by CV, GCD, electrochemical impedance spectroscopy (EIS), and cycling stability measurements in a 1 M KOH aqueous electrolyte. Fig. 5a and b present the CV curves of the $Ti_3C_2T_x$ MXene and Ni-dMXNC electrodes at various scan rates of 5, 10, 20, 30, 40, and 50 mV s^{-1} in the potential range of 0–0.8 V. All CV curves contain a pair of strong, symmetric redox peaks, displaying the electrochemical behaviour in both $Ti_3C_2T_x$ MXene and Ni-dMXNC. With increases in the scan rate, the anodic and cathodic peaks in the CV curves are

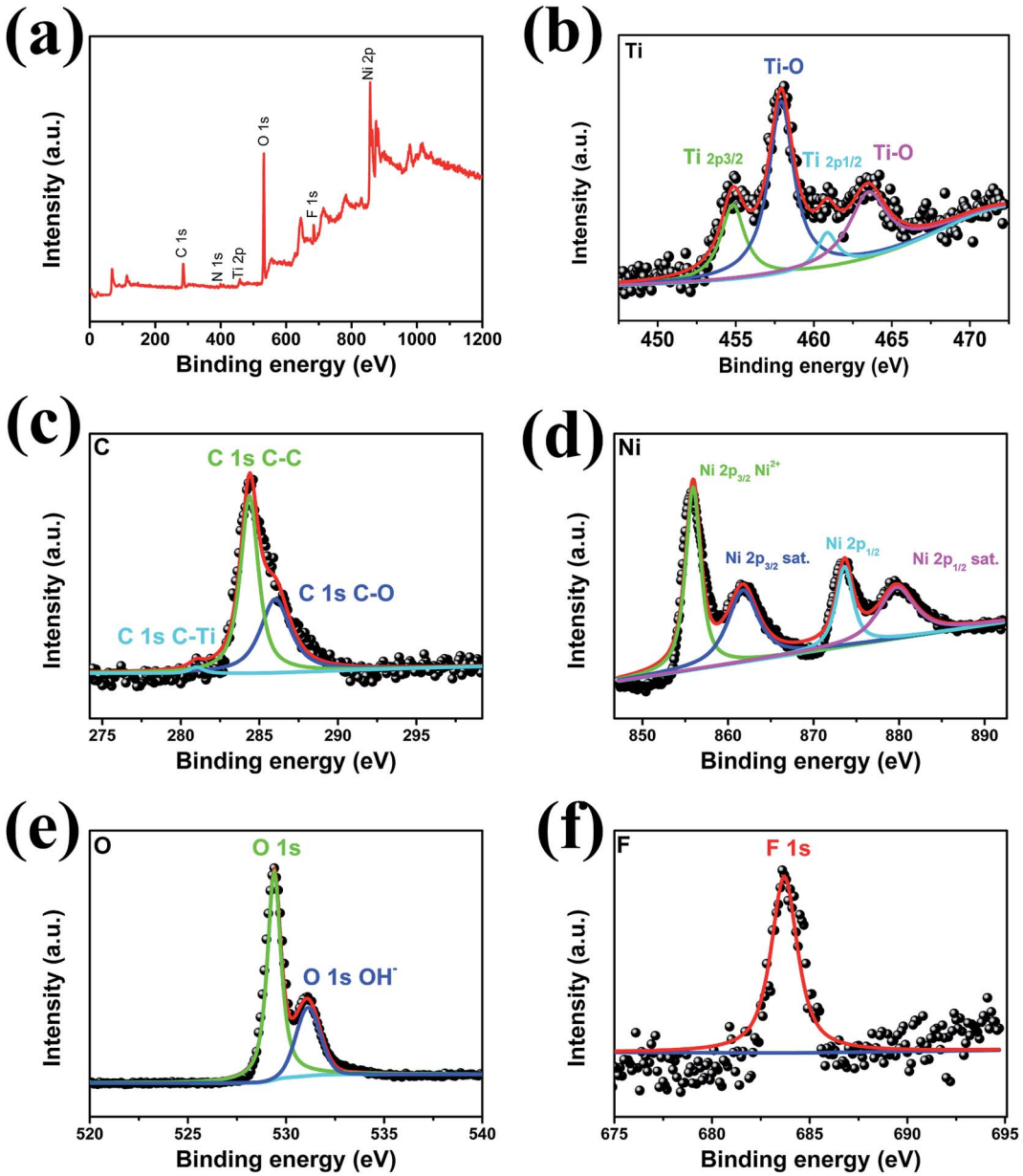

Fig. 3 (a) High-resolution XPS survey spectra. (b) Ti 2p, (c) C 1s, (d) Ni 2p, (e) O 1s, and (f) F 1s spectra of Ni-dMXNC.

shifted to the positive and negative potential sides, respectively, as further confirmed by the subsequent GCD measurements. The CV curves of the $Ti_3C_2T_x$ MXene evaluated in the potential range of −1.0 to 0 V shows a symmetrical rectangle (Fig. S6, ESI†), indicating a double electrode layer behaviour, which can be employed as a negative electrode for asymmetric supercapacitor. Fig. 5c and d highlight the GCD curves of the $Ti_3C_2T_x$ MXene and Ni-dMXNC electrodes at different current densities; both show strong faradaic capacitor behaviours.[54,55]

EIS analysis is routinely used to evaluate the ion transportability across the electrolyte/electrode interface in supercapacitor applications. The EIS analyses of the $Ti_3C_2T_x$ MXene and Ni-dMXNC electrodes were obtained from 100 kHz to 0.01 Hz using a three-electrode system (Fig. 5e and f). The impedance spectra, in the form of Nyquist plots, demonstrate sharp semicircles intersecting the real axis in the high-frequency regions and nearly vertical lines in the low-frequency regions. The high-frequency intercept (100 kHz) represent the equivalent series resistance (R_s) across the electrode/electrolyte, which reflects the contribution from the electronic, electrolyte, contact, and internal resistances of the active materials.[56] The semicircle, formed by double-layer capacity (C_{dl}) and charge-transfer resistance (R_{ct}), confirms the charge-transfer process across the electrode/electrolyte interface. At low frequency, the sloped curve, relating to the electrolyte diffusion in the active materials, reflects the Warburg resistance (Z_w).[57] The R_s, R_{ct}, and Z_w values of the $Ti_3C_2T_x$ MXene electrode are 1.057 Ω, 46.780 Ω, and 5.727 Ω, respectively, while

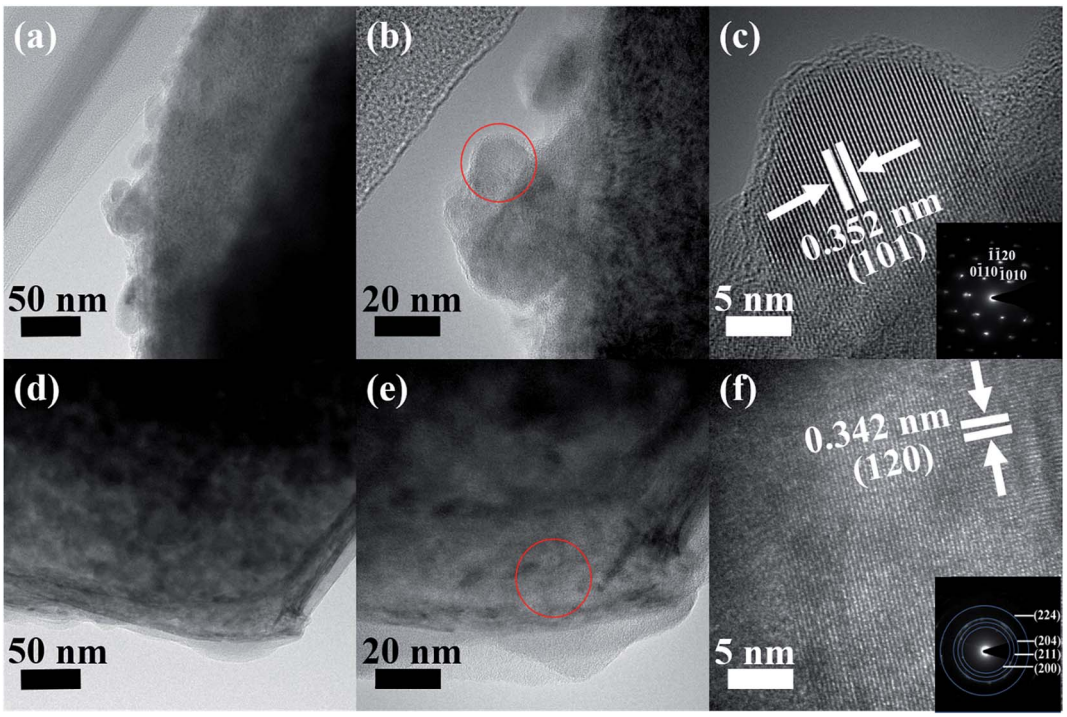

Fig. 4 (a) and (b) Low-magnification TEM image, (c) HRTEM image (red circle area in (b)), and corresponding SAED pattern (inset) of the $Ti_3C_2T_x$ MXene; (d) and (e) low-magnification TEM image, (f) HRTEM image (red circle area in (e)), and corresponding SAED pattern (inset) of the Ni-dMXNC.

Table 1 Specific surface area, pore volume and pore size of the $Ti_3C_2T_x$ MXene and Ni-dMXNC materials

Sample	Pore size (nm)	S_{BET} ($m^2\ g^{-1}$)	V_{pores} ($cm^3\ g^{-1}$)
$Ti_3C_2T_x$	24.1	10.0	0.02
Ni-dMXNC	21.1	77.5	0.20

for the Ni-dMXNC electrode these are reduced to 0.960 Ω, 0.383 Ω, and 1.653 Ω. These lower R_s and R_{ct} values of the Ni-dMXNC electrode compared to those of the $Ti_3C_2T_x$ MXene electrode indicate the higher conductivity of the former. The decreased Z_w value may be from the high surface area of the Ni-dMXNC electrode, which facilitates fast electrolyte ion diffusion to the active sites and surface of the Ni-dMXNC. The Ni-dMXNC electrode reveals a higher C_{dl} value of 3.375 F, compared to 0.066 F, than the $Ti_3C_2T_x$ MXene electrode does, indicating that the presence of the 3D porous NiO nanosheets contributes to the specific capacity of the Ni-dMXNC electrode.

In the CV spectra obtained at a scan rate of 10 mV s^{-1} of the $Ti_3C_2T_x$ MXene and Ni-dMXNC electrodes (Fig. 6a), a pair of redox peaks with an anodic peak at 0.55 V and a cathodic peak at 0.39 V is observed for the $Ti_3C_2T_x$ MXene electrode, whereas a pair of redox peaks with an anodic peak at 0.51 V and cathodic peak at 0.30 V occurs for the Ni-dMXNC electrode, indicating the presence of strong faradaic behaviour in both electrodes. Moreover, the average area under the Ni-dMXNC electrode CV curve is higher than that of the $Ti_3C_2T_x$ MXene electrode, suggesting that the Ni-dMXNC shows higher electrochemical performance than the MXene. In this case, the Ni foam acting as a current collector in the electrode produced a flat line in the CV curve, indicating that the capacity of the Ni foam is negligible.[58,59] In the diffusion-controlled electrochemical redox reaction, the peak current i_p is calculated according to the Randles–Sevcik equation:[60]

$$i_p = (2.69 \times 10^5) n^{3/2} A {D_o}^{1/2} C_o^* \nu^{1/2} \quad (7)$$

where i_p is the peak current, n is the number of electrons transferred, A is the electrode area, D_o is the diffusion coefficient, C_o^* is the reactant concentration, and ν is the scan rate. The relationships between the positive peak current ($I_{p,c}$) and the scan rate (ν) of the $Ti_3C_2T_x$ MXene and Ni-dMXNC composite electrodes are shown in Fig. 6b. $I_{p,c}$ increases linearly with $\nu^{1/2}$, confirming that the faradaic nature of both electrodes is limited by the diffusion of OH^- to the active sites. The diffusion coefficients of the Ni-dMXNC composite electrode ($D_{Ni\text{-}dMXNC}$) exhibiting higher diffusion coefficients compare with $Ti_3C_2T_x$ MXene ($D_{Ti_3C_2T_x}$). This result was further confirmed by the GCD measurements of $Ti_3C_2T_x$ MXene and Ni-dMXNC electrodes at the current density of 1 A g^{-1} (Fig. 6c). The Q_D values of $Ti_3C_2T_x$ MXene and Ni-dMXNC electrodes (Fig. 6d) were calculated from the GCD curves at current densities of 1, 2, 3, 4, 5, 8, and 10 A g^{-1}. The Q_D values of the $Ti_3C_2T_x$ and Ni-dMXNC electrodes are 8.2, 7.3, 6.6, 5.8, 5.6, 4.1 and 4.4 mA h g^{-1}, and 60.7, 56.2, 52.4, 49.5, 47.0, 39.7 and 35.6 mA h g^{-1}, respectively. The capacity of the Ni-dMXNC electrode with increasing current density from 1 to 10 A g^{-1} was retained to

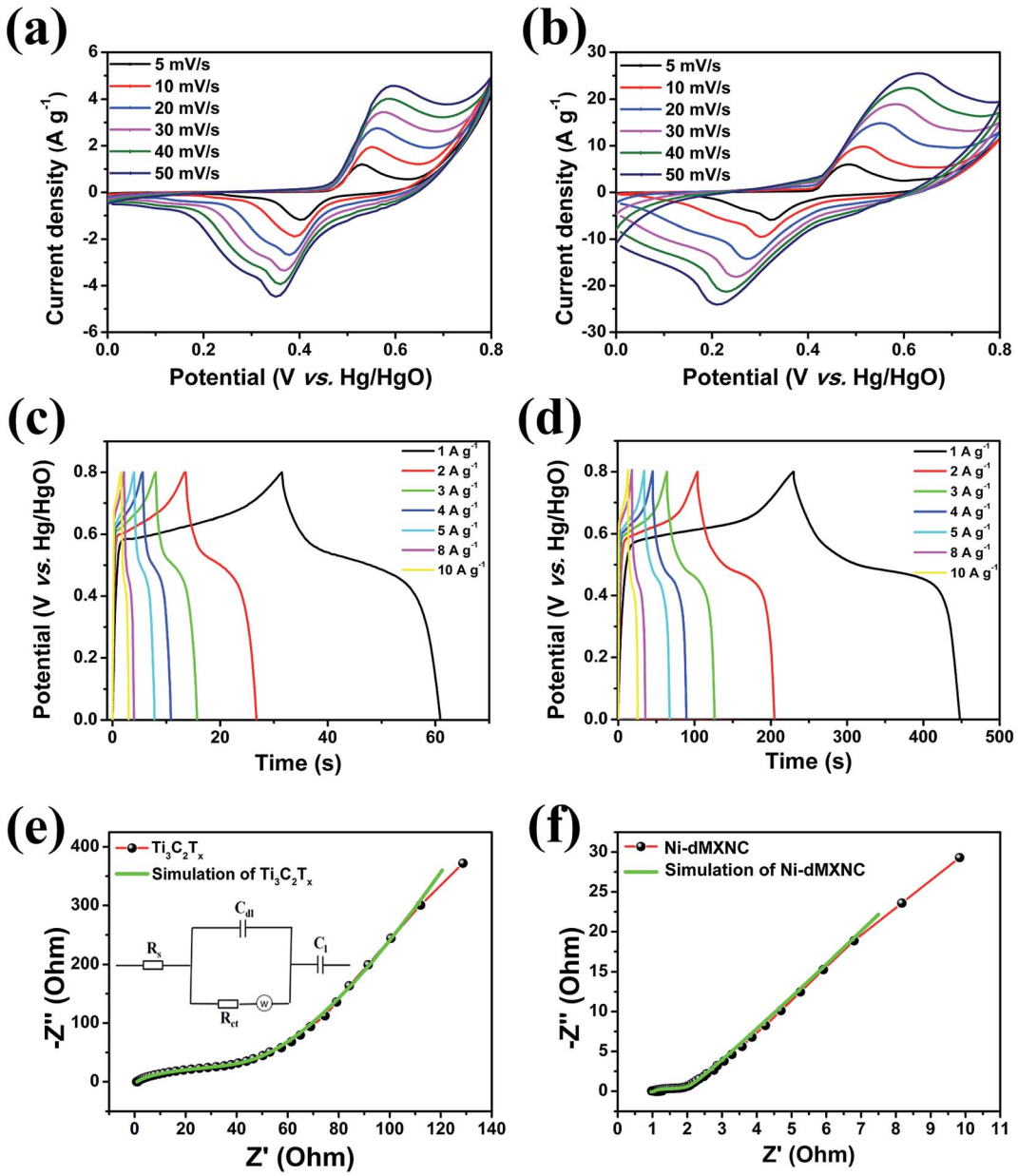

Fig. 5 CV curves of the (a) $Ti_3C_2T_x$ and (b) Ni-dMXNC electrodes at various scan rates; GCD curves of the (c) $Ti_3C_2T_x$ and (d) Ni-dMXNC electrodes at various scan rates and current densities. EIS of the (e) $Ti_3C_2T_x$ and (f) Ni-dMXNC electrodes.

58.6% based on the initial capacity value, which is higher than the 53.7% of the capacity-reduced ratio of the $Ti_3C_2T_x$ MXene electrode under the same current conditions. The specific capacity to reach 60.7 mA h g^{-1} at a current density of 1 A g^{-1}, corresponding to a volumetric specific capacity of 92.0 mA h cm^{-3}, is significantly superior to that measured on a $Ti_3C_2T_x$ MXene-based electrode (Table S2, ESI†).[20,61,62] Compared to the $Ti_3C_2T_x$ MXene electrode, the Ni-dMXNC electrode demonstrates considerably higher capacity and a better rate capability than the $Ti_3C_2T_x$ MXene electrode. This could be because of: (i) the synergistic effect generated in Ni-dMXNC by the two morphologies and porosities, as well as by the higher surface area. The presence of porous NiO between the modified $Ti_3C_2T_x$ MXene sheets could yield minimal density, relatively high out-of-plane compression properties, and good in-plane elastic properties, increasing the number of redox reactions.[63] This dual morphology of MXene and NiO is advantageous for electrolyte ion diffusion into the electrode material, while showing excellent chemical stability as confirmed by the cycling test. (ii) The functional groups on the surface of $Ti_3C_2T_x$ MXene are responsible for the enhanced faradaic capacity in the Ni-dMXNC electrode. (iii) The annealing process, which might have separated the graphite and TiO_2 to a formation of carbon-supported TiO_2 hybrids results in an enhanced conductivity and specific surface area, and increased NiO crystallization, was responsible for the decreased internal and faradaic R_{ct} values, as demonstrated in the EIS discussion. The cyclic performances of the $Ti_3C_2T_x$ MXene and Ni-dMXNC electrodes were evaluated

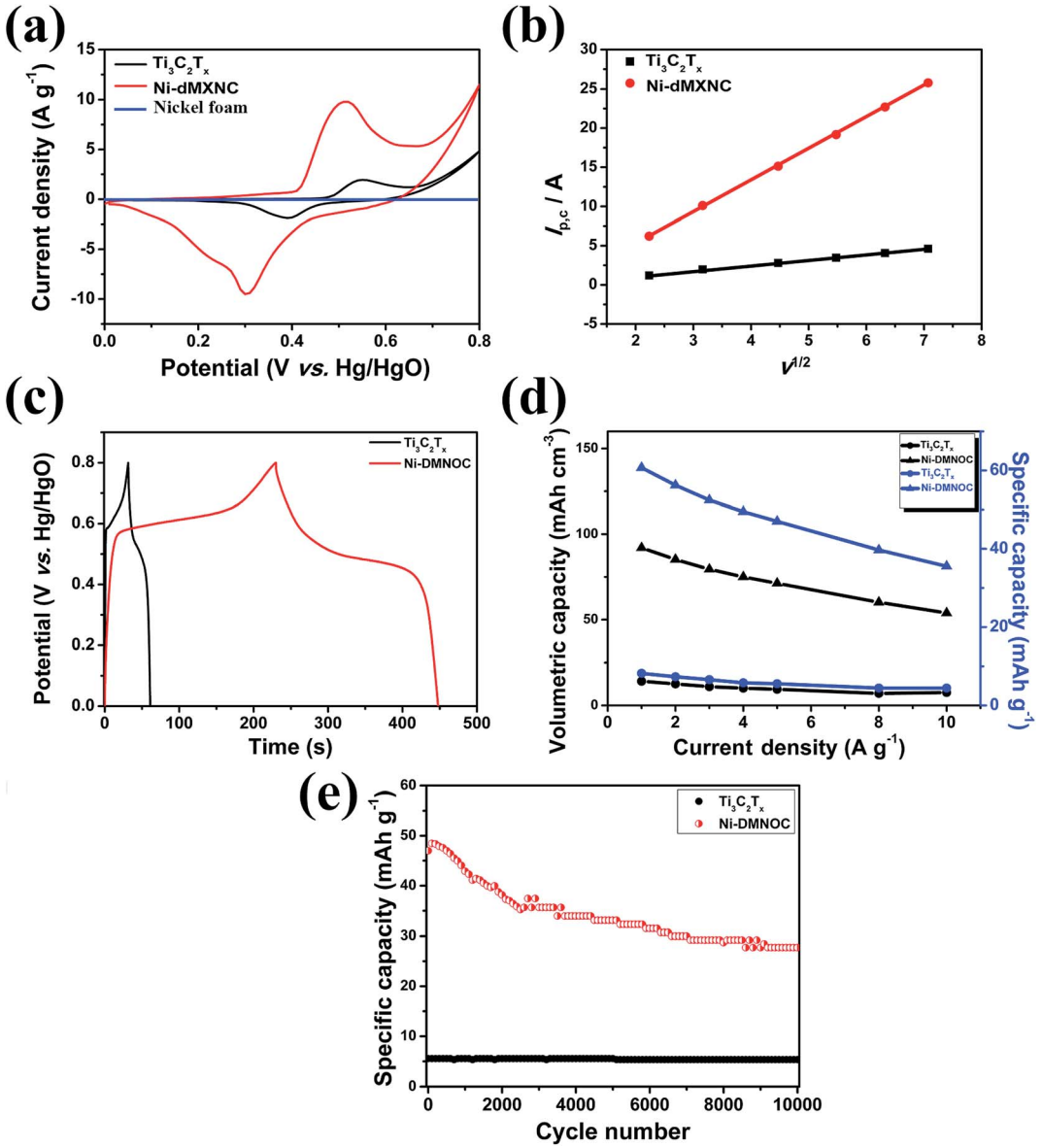

Fig. 6 (a) CV curves of the Ni foam, $Ti_3C_2T_x$ MXene, and Ni-dMXNC electrodes at a scan rate of 10 mV s^{-1}, (b) relationship between the cathodic peak current and the square root of the scan rate for $Ti_3C_2T_x$ and Ni-dMXNC electrodes. (c) Galvanostatic charge/discharge (GCD) curves of the $Ti_3C_2T_x$ and Ni-dMXNC electrodes at current density of 1 A g^{-1}, (d) comparison of the specific gravimetric capacities and volumetric capacities of the $Ti_3C_2T_x$ MXene and Ni-dMXNC electrodes at different current densities, (e) cycling performance of the $Ti_3C_2T_x$ MXene and Ni-dMXNC electrodes at a current density of 5 A g^{-1}.

for 5000 charge/discharge testing cycles at a current density of 5 A g^{-1} (Fig. 6e). The $Ti_3C_2T_x$ MXene electrode exhibited excellent cycling performance with only 3.6% degradation after 5000 cycles at a current density of 5 A g^{-1}, but was very low capacity. For the Ni-dMXNC electrode, the capacity (Q_D) was rapidly increased from 47.0 to 48.5 mA h g^{-1} to first 100 cycles due to the initial activation of the electrode, slowly dropped to 35.3 mA h g^{-1} to 2500 cycles, and stabilized to 33.1 mA h g^{-1} after 4400 cycles. The capacity retention of the Ni-dMXNC electrode after 5000 cycles exhibited a moderate improvement of about 70.4%, attributed to the decorated NiO on the $Ti_3C_2T_x$ MXene (about 64.3% retention of a pure NiO electrode after 5000 cycles as shown in Fig. S7†). For purpose of improving the capacitive properties of the positive electrode in a hybrid asymmetric cell, it would be highly desirable to boost the performance of the negative electrode. With the purpose of the capacity balance of a positive electrode and a negative electrode, it is necessary to be a suitable mass ratio of the positive electrode : negative electrode. The GCD curves of asymmetric cells with the potential change of each individual electrode *in situ* were monitored by an auxiliary channel and a reference electrode (mercury/mercury oxide) (Fig. S8†). The applied current for each electrode was kept at 1 mA. The positive electrode (Ni-dMXNC) was swept between 0 to 0.8 V, while the negative electrode ($Ti_3C_2T_x$ MXene) was scanned at 0 to −1 V. When a mass ratio of the positive and negative electrodes was 1 : 4.39, they exhibited similar capacity.

In order to evaluate the applicability of Ni-dMXNC electrodes in practical supercapacitors, we fabricated an ASC with a Ni-dMXNC positive electrode, $Ti_3C_2T_x$ negative electrode, and electrolyte of 1 M KOH (denoted as Ni-dMXNC//$Ti_3C_2T_x$), as illustrated in Fig. 7e. To achieve the maximum full-cell capacity, the charge balance followed the relation $q_+ = q_-$, where q_+ and q_- represent the positive and negative electrode charges, respectively. The charge storage was on $q = C \times \Delta E \times m$.[64] From the charge balance, the ASC device should have a positive-negative electrode mass ratio of 0.23. The electrochemical properties of the Ni-dMXNC//$Ti_3C_2T_x$ ASC were tested in a two-electrode system. Fig. 7a presents the CV curves obtained from the fabricated Ni-dMXNC//$Ti_3C_2T_x$ ASC device at different scan rates in the 0–1.8 V potential window. The faradaic capacity contribution causes a pair of evident redox peaks to appear in the curves. The charge/discharge curves obtained at various current densities are shown in Fig. 7b and suggest non-linearity because of the contributions to the redox reaction by the NiO and modified $Ti_3C_2T_x$ MXene, consistent with the CV curves. The Q_D (Fig. 7c) of the Ni-dMXNC//$Ti_3C_2T_x$ ASC device was 4.7,

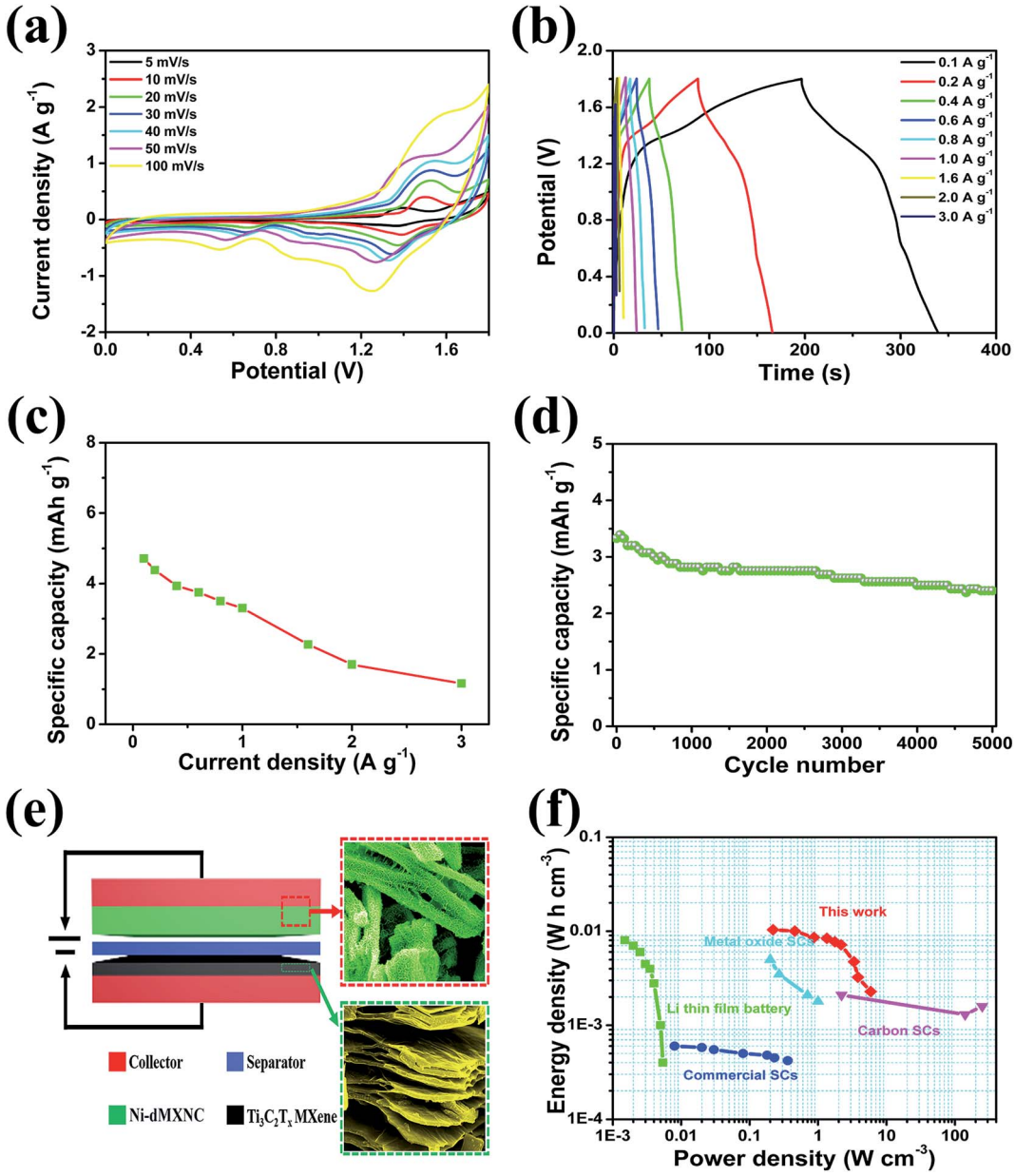

Fig. 7 (a) CV curves of Ni-dMXNC//$Ti_3C_2T_x$ asymmetric supercapacitor at different scan rates; (b) GCD curves of Ni-dMXNC//$Ti_3C_2T_x$ asymmetric supercapacitor; (c) capacity retention of Ni-dMXNC//$Ti_3C_2T_x$ asymmetric supercapacitor at different current densities; (d) cycling performance of the Ni-dMXNC//$Ti_3C_2T_x$ asymmetric supercapacitor at a current density of 1 A g^{-1}; (e) schematic of the Ni-dMXNC//$Ti_3C_2T_x$ asymmetric supercapacitor configuration with each SEM image; (f) Ragone plot of Ni-dMXNC//$Ti_3C_2T_x$ ASCs. The comparison of energy and power density of Ni-dMXNC//$Ti_3C_2T_x$ ASCs, Li thin film battery,[65] metal oxide,[31] commercial SC,[66] and carbon micro-SCs,[65,67] demonstrating that Ni-dMXNC//$Ti_3C_2T_x$ ASCs exhibit exceptional electrochemical energy storage with simultaneous high energy density and power density.

4.4, 3.9, 3.8, 3.5, 3.3, 2.3, 1.7 and 1.2 mA h g^{-1} at current densities of 0.1, 0.2, 0.4, 0.6, 0.8, 1.0, 1.6, 2.0 and 3.0 A g^{-1}, respectively (based on the total mass of each electrode in a device). To further investigate the cycling stability of the ASC device, the cycling performances within 0–1.8 V at a current density of 1 A g^{-1} were observed over 5000 cycles. In first 800 cycles, the Q_D tended to decreases rapidly as NiO may be activated by KOH electrolyte (Fig. 7d). In subsequent cycles, the capacity of the ASC device dropped smoothly and exhibited a 72.1% retention rate after 5000 cycles. In a Ragone plot shown in Fig. 7f, an ASC device consisting of Ni-dMXNC as a positive electrode and $Ti_3C_2T_x$ as a negative electrode delivered an energy density of 1.04×10^{-2} W h cm^{-3} at a power density of 0.22 W cm^{-3}. When the power density was 5.88 W cm^{-3}, the energy density was 2.29×10^{-3} W h cm^{-3}. The energy density value calculated based on the volume of active electrodes is much higher than most reported Li thin film battery,[65] metal oxide based SCs,[31] commercial SC,[66] carbon-based micro-SCs.[65,67] Moreover, it's comparable to the areal energy/power density of $NiCo_2S_4$//CNF hybrid device and clay-like Ti_3C_2 MXene MSCs.[68,69] To demonstrate the application potential of the Ni-dMXNC//$Ti_3C_2T_x$ ASC device, we connected two ASC coin cells in series to drive a red light-emitting diode for 12 min (Fig. 7f (inset)). The long-term ON performance is attributed to the Ni-dMXNC structure and the unique 3D morphology, which could provide numerous channels to enhance the ion transport kinetics across the electrode–electrolyte interface. Ni-dMXNC could also permit electrolyte ions to intercalate/deintercalate without structural distortion, as demonstrated by the good cycling stability. These results show that Ni-dMXNC may be a promising positive electrode material for ASCs in the future.

4. Conclusions

A highly hierarchical porous honeycomb-like structure of NiO nanosheets was successfully grown on the surface of $Ti_3C_2T_x$ MXene by a facile and efficient hydrothermal method. $Ti_3C_2T_x$ MXene showed typical delamination of the MXene structure, with thicknesses of 40–200 nm. The as-obtained Ni-dMXNC electrode showed a remarkably high specific capacity of 60.7 mA h g^{-1} at 1 A g^{-1}, corresponding to a volumetric specific capacity of 92.0 mA h cm^{-3}, and a good capacity retention rate. The proposed Ni-dMXNC//$Ti_3C_2T_x$ ASC exhibited a higher energy density of 1.04×10^{-2} W h cm^{-3} at a power density of 0.22 W cm^{-3} based on the total volume of active materials than those of most previously reported $Ti_3C_2T_x$-based ASCs and other typical ASCs. The superior electrochemical performance was attributed to the presence of the high-surface-area multilayers of Ni-dMXNC nanostructures.

This work demonstrates that the as-obtained Ni-dMXNC nanostructures are promising electrode materials for the further development of high-performance energy-storage devices.

Acknowledgements

This study was supported by the Global Frontier Program through the Global Frontier Hybrid Interface Materials (GFHIM) of the National Research Foundation of Korea (NRF) funded by the Ministry of Science, ICT & Future Planning (2013M3A6B1078874).

References

1 K. Novoselov, D. Jiang, F. Schedin, T. Booth, V. Khotkevich, S. Morozov and A. Geim, *Proc. Natl. Acad. Sci. U. S. A.*, 2005, **102**, 10451–10453.
2 K. S. Novoselov, A. K. Geim, S. Morozov, D. Jiang, Y. Zhang, S. a. Dubonos, I. Grigorieva and A. Firsov, *Science*, 2004, **306**, 666–669.
3 M. Naguib, V. N. Mochalin, M. W. Barsoum and Y. Gogotsi, *Adv. Mater.*, 2014, **26**, 992–1005.
4 Q. H. Wang, K. Kalantar-Zadeh, A. Kis, J. N. Coleman and M. S. Strano, *Nat. Nanotechnol.*, 2012, **7**, 699–712.
5 F. Bonaccorso, Z. Sun, T. Hasan and A. Ferrari, *Nat. Photonics*, 2010, **4**, 611–622.
6 M. Naguib, M. Kurtoglu, V. Presser, J. Lu, J. Niu, M. Heon, L. Hultman, Y. Gogotsi and M. W. Barsoum, *Adv. Mater.*, 2011, **23**, 4248–4253.
7 C. Zhang, H. Yin, M. Han, Z. Dai, H. Pang, Y. Zheng, Y.-Q. Lan, J. Bao and J. Zhu, *ACS Nano*, 2014, **8**, 3761–3770.
8 C. Liu, Z. Yu, D. Neff, A. Zhamu and B. Z. Jang, *Nano Lett.*, 2010, **10**, 4863–4868.
9 Y. Wang, Z. Q. Shi, Y. Huang, Y. F. Ma, C. Y. Wang, M. M. Chen and Y. S. Chen, *J. Phys. Chem. C*, 2009, **113**, 13103–13107.
10 C. G. Liu, Z. N. Yu, D. Neff, A. Zhamu and B. Z. Jang, *Nano Lett.*, 2010, **10**, 4863–4868.
11 M. Naguib, O. Mashtalir, J. Carle, V. Presser, J. Lu, L. Hultman, Y. Gogotsi and M. W. Barsoum, *ACS Nano*, 2012, **6**, 1322–1331.
12 B. Radisavljevic, A. Radenovic, J. Brivio, V. Giacometti and A. Kis, *Nat. Nanotechnol.*, 2011, **6**, 147–150.
13 H. Liu, A. T. Neal, Z. Zhu, Z. Luo, X. Xu, D. Tománek and P. D. Ye, *ACS Nano*, 2014, **8**, 4033–4041.
14 K. Novoselov, A. K. Geim, S. Morozov, D. Jiang, M. Katsnelson, I. Grigorieva, S. Dubonos and A. Firsov, *Nature*, 2005, **438**, 197–200.
15 M. W. Barsoum, *MAX phases: properties of machinable ternary carbides and nitrides*, John Wiley & Sons, 2013.
16 M. W. Barsoum, *Prog. Solid State Chem.*, 2000, **28**, 201–281.
17 M. Kurtoglu, M. Naguib, Y. Gogotsi and M. W. Barsoum, *MRS Commun.*, 2012, **2**, 133–137.
18 D. Er, J. Li, M. Naguib, Y. Gogotsi and V. B. Shenoy, *ACS Appl. Mater. Interfaces*, 2014, **6**, 11173–11179.
19 Q. Tang, Z. Zhou and P. Shen, *J. Am. Chem. Soc.*, 2012, **134**, 16909–16916.
20 M. R. Lukatskaya, O. Mashtalir, C. E. Ren, Y. Dall'Agnese, P. Rozier, P. L. Taberna, M. Naguib, P. Simon, M. W. Barsoum and Y. Gogotsi, *Science*, 2013, **341**, 1502–1505.
21 M. D. Levi, M. R. Lukatskaya, S. Sigalov, M. Beidaghi, N. Shpigel, L. Daikhin, D. Aurbach, M. W. Barsoum and Y. Gogotsi, *Adv. Energy Mater.*, 2015, **5**, 1400815.
22 P. Simon and Y. Gogotsi, *Nat. Mater.*, 2008, **7**, 845–854.

23 Y. W. Zhu, S. Murali, M. D. Stoller, K. J. Ganesh, W. W. Cai, P. J. Ferreira, A. Pirkle, R. M. Wallace, K. A. Cychosz, M. Thommes, D. Su, E. A. Stach and R. S. Ruoff, *Science*, 2011, **332**, 1537–1541.
24 J. Yan, Q. Wang, T. Wei and Z. J. Fan, *Adv. Energy Mater.*, 2014, **4**, 1300816–1300859.
25 R. Rakhi, B. Ahmed, M. Hedhili, D. H. Anjum and H. N. Alshareef, *Chem. Mater.*, 2015, **27**, 5314–5323.
26 S. Y. Lin and X. Zhang, *J. Power Sources*, 2015, **294**, 354–359.
27 M. Ghidiu, M. R. Lukatskaya, M. Q. Zhao, Y. Gogotsi and M. W. Barsoum, *Nature*, 2014, **516**, 78–81.
28 Y. Gogotsi and P. Simon, *Science*, 2011, **334**, 917–918.
29 Q. Wang, J. Yan and Z. Fan, *Energy Environ. Sci.*, 2016, **9**, 729–762.
30 M. Ghaffari, Y. Zhou, H. Xu, M. Lin, T. Y. Kim, R. S. Ruoff and Q. Zhang, *Adv. Mater.*, 2013, **25**, 4879–4885.
31 Y. Y. Peng, B. Akuzum, N. Kurra, M. Q. Zhao, M. Alhabeb, B. Anasori, E. C. Kumbur, H. N. Alshareef, M.-D. Ger and Y. Gogotsi, *Energy Environ. Sci.*, 2016, **9**, 2847–2854.
32 M. Naguib, O. Mashtalir, M. R. Lukatskaya, B. Dyatkin, C. Zhang, V. Presser, Y. Gogotsi and M. W. Barsoum, *Chem. Commun.*, 2014, **50**, 7420–7423.
33 Q. Xia, K. S. Hui, K. Hui, D. Hwang, S. Lee, W. Zhou, Y. Cho, S. Kwon, Q. Wang and Y. Son, *Mater. Lett.*, 2012, **69**, 69–71.
34 A. Laheäär, P. Przygocki, Q. Abbas and F. Béguin, *Electrochem. Commun.*, 2015, **60**, 21–25.
35 Z. Li, Z. Xu, H. Wang, J. Ding, B. Zahiri, C. M. Holt, X. Tan and D. Mitlin, *Energy Environ. Sci.*, 2014, **7**, 1708–1718.
36 L. Q. Mai, A. Minhas-Khan, X. Tian, K. M. Hercule, Y. L. Zhao, X. Lin and X. Xu, *Nat. Commun.*, 2013, **4**, 2923–2930.
37 Z. Ling, C. E. Ren, M. Q. Zhao, J. Yang, J. M. Giammarco, J. Qiu, M. W. Barsoum and Y. Gogotsi, *Proc. Natl. Acad. Sci. U. S. A.*, 2014, **111**, 16676–16681.
38 C. J. Zhang, S. J. Kim, M. Ghidiu, M. Q. Zhao, M. W. Barsoum, V. Nicolosi and Y. Gogotsi, *Adv. Funct. Mater.*, 2016, **26**, 4143–4151.
39 X. Lu, G. Wang, T. Zhai, M. Yu, J. Gan, Y. Tong and Y. Li, *Nano Lett.*, 2012, **12**, 1690–1696.
40 H. Kim, M. Y. Cho, M. H. Kim, K. Y. Park, H. Gwon, Y. Lee, K. C. Roh and K. Kang, *Adv. Energy Mater.*, 2013, **3**, 1500–1506.
41 B. H. Dang, M. Rahman, D. MacElroy and D. P. Dowling, *Surf. Coat. Technol.*, 2012, **206**, 4113–4118.
42 M. Hassan, R. Rawat, P. Lee, S. Hassan, A. Qayyum, R. Ahmad, G. Murtaza and M. Zakaullah, *Appl. Phys. A*, 2008, **90**, 669–677.
43 J. Halim, K. M. Cook, M. Naguib, P. Eklund, Y. Gogotsi, J. Rosen and M. W. Barsoum, *Appl. Surf. Sci.*, 2016, **362**, 406–417.
44 G. Liu, C. Han, M. Pelaez, D. Zhu, S. Liao, V. Likodimos, N. Ioannidis, A. G. Kontos, P. Falaras and P. S. Dunlop, *Nanotechnology*, 2012, **23**, 294003.
45 W. S. Epling, G. B. Hoflund, J. F. Weaver, S. Tsubota and M. Haruta, *J. Phys. Chem.*, 1996, **100**, 9929–9934.
46 M. M. O. Thotiyl, S. A. Freunberger, Z. Peng, Y. Chen, Z. Liu and P. G. Bruce, *Nat. Mater.*, 2013, **12**, 1050–1056.
47 X. Liang, A. Garsuch and L. F. Nazar, *Angew. Chem., Int. Ed.*, 2015, **54**, 3907–3911.
48 D. R. Mitchell, *Ultramicroscopy*, 2008, **108**, 367–374.
49 Y. Liu, X. Zhang, S. Dong, Z. Ye and Y. Wei, *J. Mater. Sci.*, 2017, **52**, 2200–2209.
50 K. Hantanasirisakul, M. Q. Zhao, P. Urbankowski, J. Halim, B. Anasori, S. Kota, C. E. Ren, M. W. Barsoum and Y. Gogotsi, *Adv. Electron. Mater.*, 2016, **6**, 1600050–1600057.
51 M. Li, J. Ding and J. Xue, *J. Mater. Chem. A*, 2013, **1**, 7469–7476.
52 H. Zhu, J. Yin, X. Wang, H. Wang and X. Yang, *Adv. Funct. Mater.*, 2013, **23**, 1305–1312.
53 H. Zhang, X. Yu and P. V. Braun, *Nat. Nanotechnol.*, 2011, **6**, 277–281.
54 S. Yu, N. Yang, H. Zhuang, S. Mandal, O. Williams, B. Yang, N. Huang and X. Jiang, *J. Mater. Chem. A*, 2017, **5**, 1778–1785.
55 T. Brousse, D. Bélanger and J. W. Long, *J. Electrochem. Soc.*, 2015, **162**, A5185–A5189.
56 G. Yu, L. Hu, M. Vosgueritchian, H. Wang, X. Xie, J. R. McDonough, X. Cui, Y. Cui and Z. Bao, *Nano Lett.*, 2011, **11**, 2905–2911.
57 Y. Huang, Y. Li, Z. Hu, G. Wei, J. Guo and J. Liu, *J. Mater. Chem. A*, 2013, **1**, 9809–9813.
58 W. Wang, S. Guo, M. Penchev, I. Ruiz, K. N. Bozhilov, D. Yan, M. Ozkan and C. S. Ozkan, *Nano Energy*, 2013, **2**, 294–303.
59 Z. Wu, X. L. Huang, Z. L. Wang, J. J. Xu, H. G. Wang and X. B. Zhang, *Sci. Rep.*, 2014, **4**, 3669–3677.
60 L. L. Li, W. M. Zhang, Q. Yuan, Z. X. Li, C. J. Fang, L. D. Sun, L. J. Wan and C. H. Yan, *Cryst. Growth Des.*, 2008, **8**, 4165–4172.
61 O. Mashtalir, M. Lukatskaya, A. Kolesnikov, E. Raymundo-Piñero, M. Naguib, M. Barsoum and Y. Gogotsi, *Nanoscale*, 2016, **8**, 9128–9133.
62 M. Q. Zhao, C. E. Ren, Z. Ling, M. R. Lukatskaya, C. Zhang, K. L. Van Aken, M. W. Barsoum and Y. Gogotsi, *Adv. Mater.*, 2015, **27**, 339–345.
63 C. Wu, S. Deng, H. Wang, Y. Sun, J. Liu and H. Yan, *ACS Appl. Mater. Interfaces*, 2014, **6**, 1106–1112.
64 J. Chang, M. Jin, F. Yao, T. H. Kim, V. T. Le, H. Yue, F. Gunes, B. Li, A. Ghosh and S. Xie, *Adv. Funct. Mater.*, 2013, **23**, 5074–5083.
65 D. Pech, M. Brunet, H. Durou, P. Huang, V. Mochalin, Y. Gogotsi, P. L. Taberna and P. Simon, *Nat. Nanotechnol.*, 2010, **5**, 651–654.
66 D. Yu, K. Goh, Q. Zhang, L. Wei, H. Wang, W. Jiang and Y. Chen, *Adv. Mater.*, 2014, **26**, 6790–6797.
67 M. F. El-Kady and R. B. Kaner, *Nat. Commun.*, 2013, **4**, 1475–1484.
68 Q. Jiang, N. Kurra, C. Xia and H. N. Alshareef, *Adv. Energy Mater.*, 2016, 1601257–1601266.
69 N. Kurra, B. Ahmed, Y. Gogotsi and H. N. Alshareef, *Adv. Energy Mater.*, 2016, **24**, 1601372–1601380.